Supplementary Materials

Graphene-supported polyoxometalate entrapped in MIL-88A network with highly efficient conversion of polysulfides in Li-S batteries

Xin-Yang Dong,[a] Ming-Liang Wang,[a] Yi Feng,[a] Jia-Yuan Zhang,[a] Yun-Dong Cao,[a] Guang-Gang Gao,*[a] Yu-Xi Zhang,[a] Lin-Lin Fan*[a]

Collaborative Innovation Center of Metal Nanoclusters & Photo/Electro-Catalysis and Sensing, School of Materials Science and Engineering, University of Jinan, 250022, Jinan, China.

*Corresponding authors

E-mail: mse_gaogg@ujn.edu.cn (Guanggang Gao); mse_fanll@ujn.edu.cn (Linlin Fan).

Experiment section

Chemical reagents and materials

1,3-dioxolane (DOL), 1,2-dimethoxyethane (DME), lithium sulfide (Li_2S), lithium bis(trifluoromethanesulfonyl) imide (LiTFSI), carbon black (CB, Super-P), polyvinylidene difluoride (PVDF) and lithium nitrate ($LiNO_3$) were bought from Sigma-Aldrich. Graphite, fumaric acid, isopropanol, N,N-dimethyformamide (DMF), $Fe(NO_3)_3 \cdot 6H_2O$, $Co(NO_3)_2 \cdot 6H_2O$, Nmethyl-2-pyrrolidinone (NMP), isopropyl alcohol, ethylene glycol, concentrated nitric acid, potassium bromide (KBr) and absolute ethanol were purchased from Sinopharm Chemical Reagent Co. Ltd. Phosphotungstic acid ($H_3PW_{12}O_{40} \cdot xH_2O$), sodium tungstate dihydrate ($Na_2WO_4 \cdot 2H_2O$), dibasic sodium phosphate (Na_2HPO_4), sodium metavanadate ($NaVO_3$) and sublimed sulfur were obtained from Aladdin.

Synthesis of MIL-88A(FeCo)

2 mmol $Fe(NO_3)_3 \cdot 6H_2O$, 2 mmol $Co(NO_3)_2 \cdot 6H_2O$, and 5 mmol fumaric acid were dissolved in 100 mL DMF and stirred at 75 °C for 4 h. After cooling down to room temperature, the samples were then centrifuged at 10000 rpm for 5 min and washed with distilled water and ethanol, and finally dried at 60 °C for 8 h in a vacuum drying oven.

Electrochemical measurements

The working electrode was synthesized by mixing sulfur composites (70 wt%), Super-P (20 wt%), and PVDF (10 wt%) in NMP solvent. The electrode slurry was coated onto aluminum foil and dried at 60 ℃ overnight. Then, the electrodes were punched into 10 mm disks in diameter, and the electrode loading of sulfur was about 1.5 mg cm^{-2}. CR2032 coin cells were assembled to test the electrochemical performance. The electrolyte contained 1.0 M LiTFSI dissolved in the binary solvent of DOL and DME (1:1 in volume) with 1.0 wt% $LiNO_3$. The amount of the electrolyte was strictly controlled for performance evaluation in the coin cells, and the cell

contained an electrolyte to sulfur (E/S) ratio of 13 mL g^{-1}. The cells were tested with constant current charge-discharge cycles on Neware battery test system between 1.7 and 2.8 V (*vs.* Li^+/Li). Electrochemical impedance spectroscopy (EIS) and cyclic voltammetry (CV) tests were performed on a CHI 660E electrochemistry workstation (ChenHua, China). Galvanostatic intermittent titration technique (GITT) tests were performed on Neware battery test system. In addition, the electrolyte was replaced with 10 μL Li_2S_6 (0.5 M) during the preparation of the symmetric cells.

Physical characterization

The morphologies of samples were analyzed by scanning electron microscope (SEM, FEG-250, 30 kV) and transmission electron microscope (TEM, JEM-2100F, 200 kV) equipped with an energy dispersive spectroscope. The structures of the samples were identified by X-ray diffraction (XRD, DX-2700). The chemical compositions and surface element states of the samples were carried out by X-ray photoelectron spectroscopy (XPS, VG ESCALAB MK II). Fourier transform infrared spectroscopy (FTIR) were obtained using a NEXUS-870 spectrophotometer with KBr pellets. Thermogravimetric analysis (TGA, Pyris Diamond6000 TG/DTA, PerkinElmer Co, America) was conducted to verify sulfur and rGO contents. Ultraviolet-visible (UV-vis) absorption spectra were conducted via UV spectrophotometer (UV-8000S Shanghai Yuanxi). The P, W, V, Fe, and Co contents were determined by inductively coupled plasma optical emission spectrometer (ICP-OES, Thermo iCAP 6300). Microanalysis of the composites was carried out using a Heraeus CHN-O-FLASH EA 1112 elemental analyzer. The specific surface area of samples was determined by the Brunauer-Emmett-Teller (BET) nitrogen adsorption/desorption method (Quadrasorb SI-MP, Quantachrome).

Lithium polysulfide adsorption measurements

Firstly, Li_2S_6 solution was prepared by dissolving Li_2S and S (at a molar ratio of 1:5) in the solution of DOL/DME (1:1 by volume), and then stirred at 65 ℃ for 24 h. Subsequently, 3 mg M88A/rGO, PW_{12}-M88A/rGO, $PW_{11}V$-M88A/rGO, and $PW_{10}V_2$-M88A/rGO were immersed into 3 mL Li_2S_6 solution under stirring for 6 h, respectively.

The adsorption capacity of the samples was investigated by XPS and UV-vis spectra.

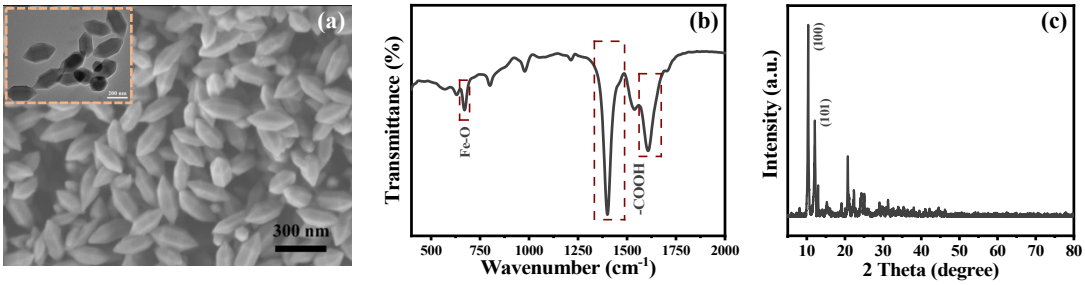

Fig. S1 (a) SEM image of M88A (the insert is TEM image). (b) FTIR spectra and (c) XRD pattern of M88A.

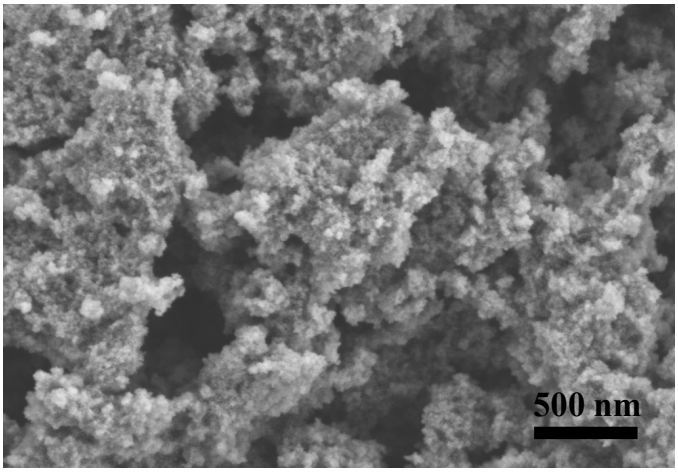

Fig. S2 SEM image of PW_9V_3-M88A.

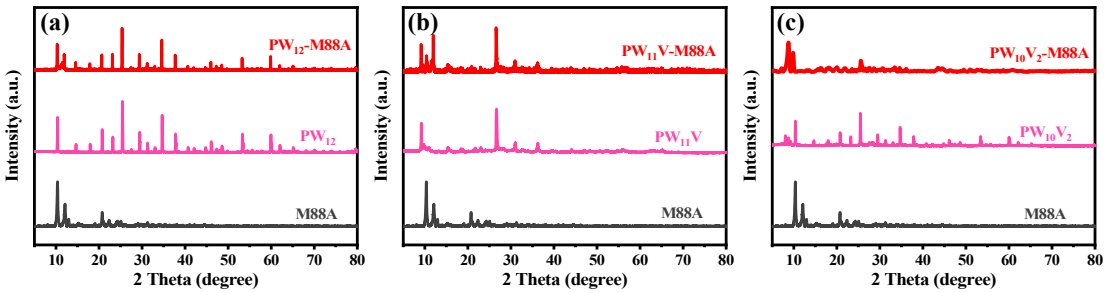

Fig. S3 XRD patterns of M88A, POMs, and POMs-M88A.

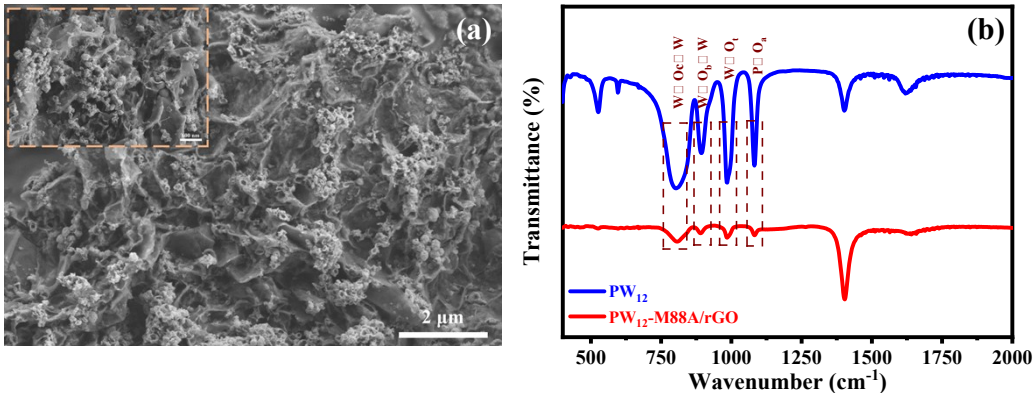

Fig. S4 (a) SEM images of PW_{12}-M88A/rGO. (b) FTIR spectra of PW_{12} and PW_{12}-M88A/rGO (O_a denotes an O atom bound to three W atoms and one P atom, O_t denotes the terminal O atoms, O_b denotes the corner-bridged O atoms, and O_c denotes the side-bridged O atoms).

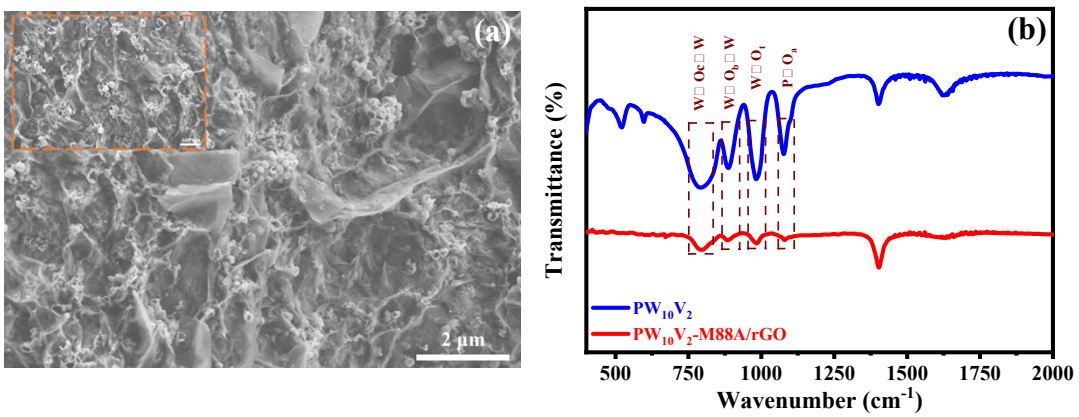

Fig. S5 (a) SEM images of $PW_{10}V_2$-M88A/rGO. (b) FTIR spectra of $PW_{10}V_2$ and $PW_{10}V_2$-M88A/rGO (O_a denotes an O atom bound to three W atoms and one P atom, O_t denotes the terminal O atoms, O_b denotes the corner-bridged O atoms, and O_c denotes the side-bridged O atoms).

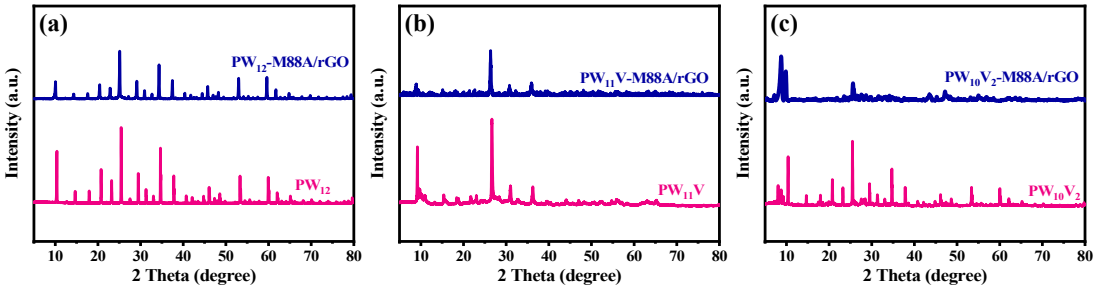

Fig. S6 XRD patterns of POMs and POMs-M88A/rGO.

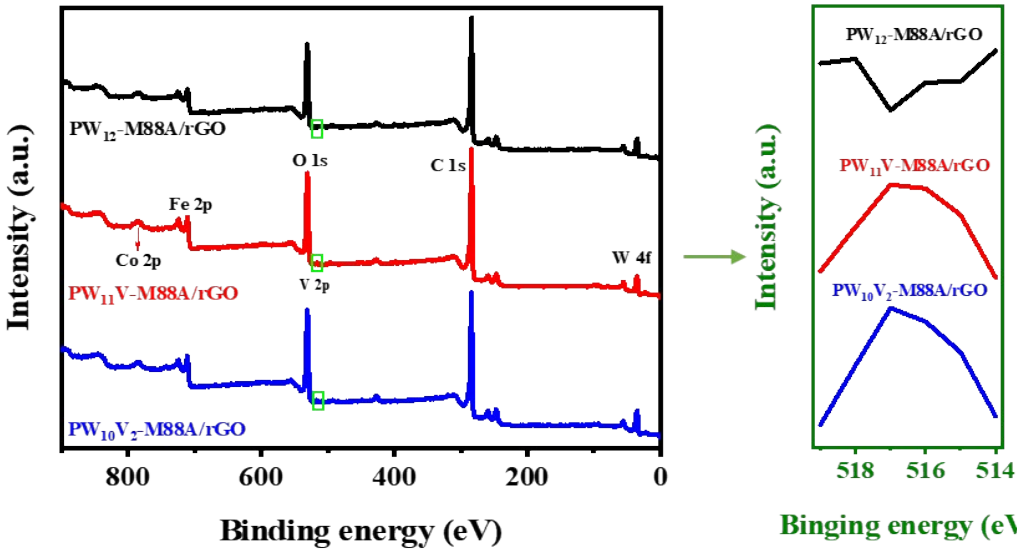

Fig. S7 The survey spectra XPS analysis of PW_{12}-M88A/rGO, $PW_{11}V$-M88A/rGO, and $PW_{10}V_2$-M88A/rGO.

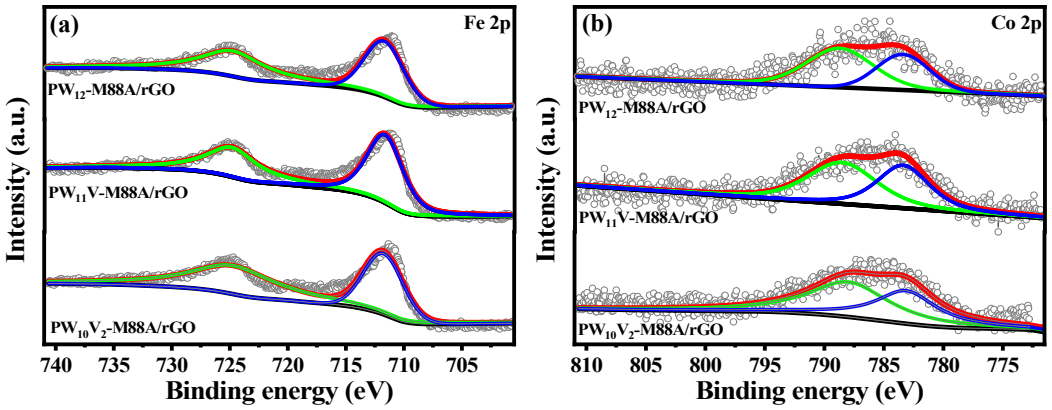

Fig. S8 XPS analysis of PW_{12}-M88A/rGO, $PW_{11}V$-M88A/rGO, and $PW_{10}V_2$-M88A/rGO: (a) Fe 2p spectra and (b) Co 2p spectra.

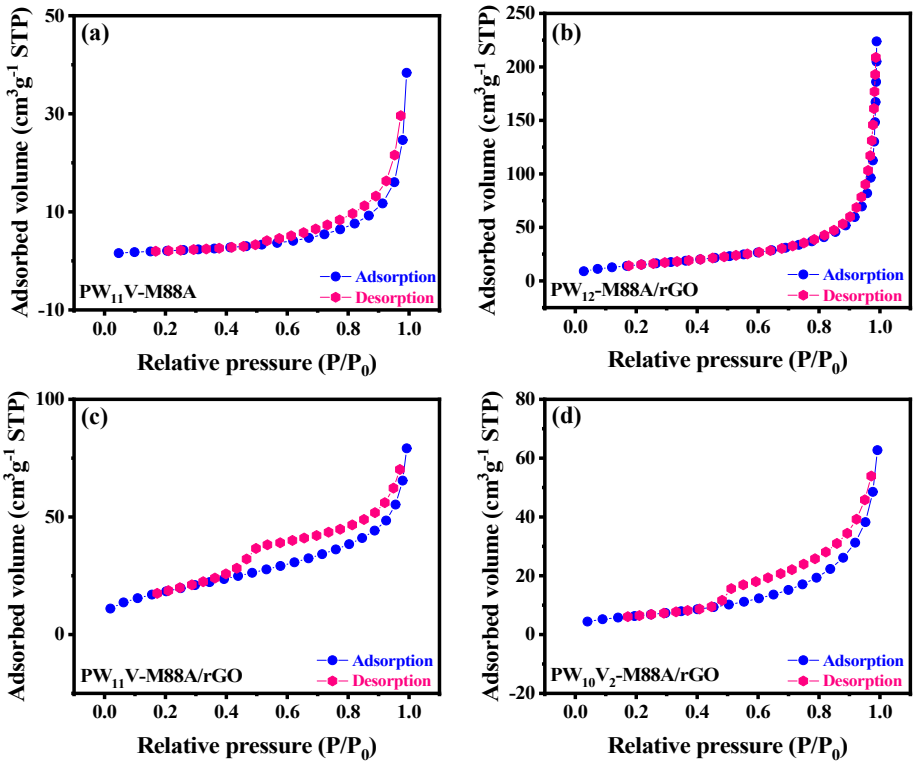

Fig. S9 N_2 adsorption-desorption isotherms of (a) $PW_{11}V$-M88A, (b) PW_{12}-M88A/rGO, (c) $PW_{11}V$-M88A/rGO, and (d) $PW_{10}V_2$-M88A/rGO.

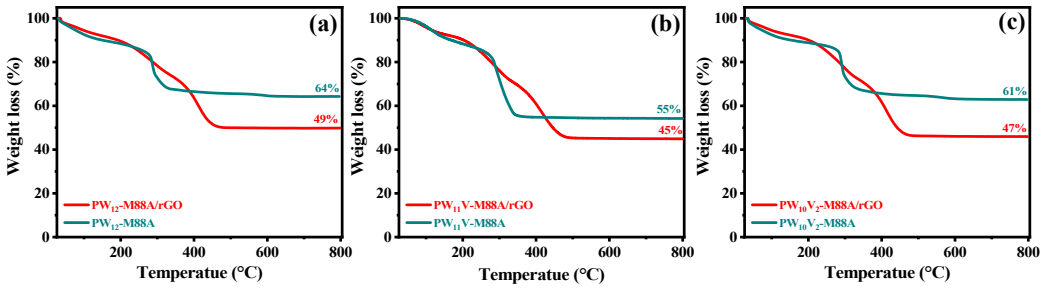

Fig. S10 TGA curves of (a) PW_{12}-M88A and PW_{12}-M88A/rGO, (b) $PW_{11}V$-M88A and $PW_{11}V$-M88A/rGO, and (c) $PW_{10}V_2$-M88A and $PW_{10}V_2$-M88A/rGO.

Taking $PW_{11}V$-M88A and $PW_{11}V$-M88A/rGO as examples. During the TGA measurement in air flow, the $PW_{11}V$-M88A and $PW_{11}V$-M88A/rGO respectively remain 55% and 45% when the temperature gradually rises from room temperature to 800 °C. If one thinks that the content of rGO in $PW_{11}V$-M88A/rGO is x%, then the content of $PW_{11}V$-M88A is (1 − x%). The following equation can be obtained: (1 − x%) × 55% = 45%, and the content of rGO in $PW_{11}V$-M88A/rGO is approximately calculated to be 18.2%.

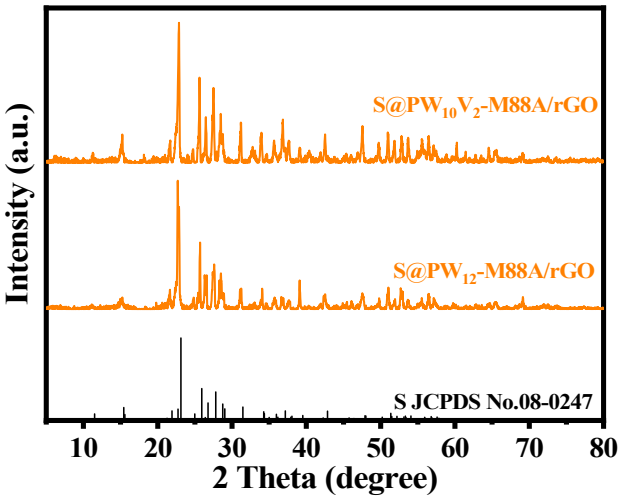

Fig. S11 XRD patterns of S@PW_{12}-M88A/rGO and S@$PW_{10}V_2$-M88A/rGO.

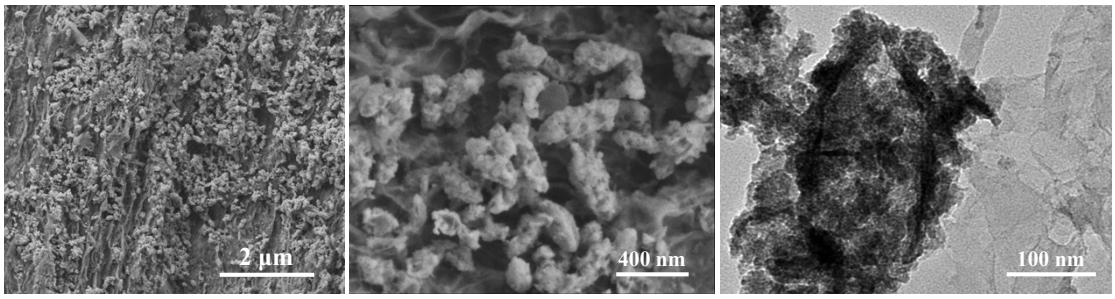

Fig. S12 SEM and TEM images of S@PW_{11}V-M88A/rGO.

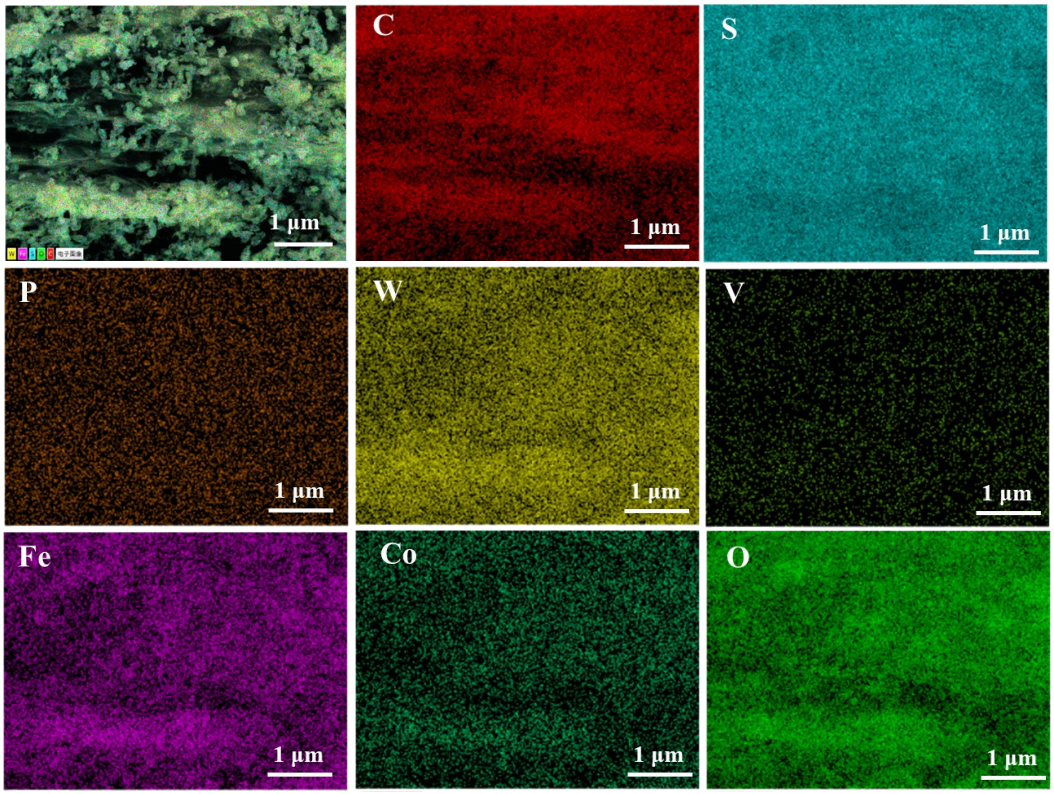

Fig. S13 The elemental mapping of C, S, P, W, V, Fe, Co, and O of S@PW_{11}V-M88A/rGO.

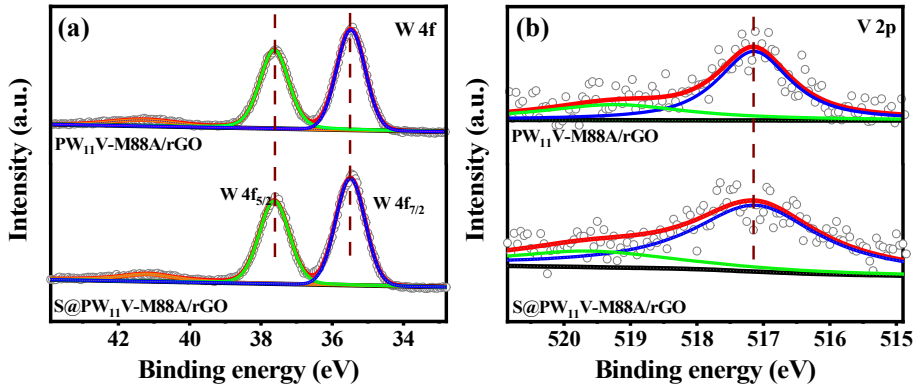

Fig. S14 XPS analysis of $PW_{11}V$-M88A/rGO and S@$PW_{11}V$-M88A/rGO: (a) W 4f spectra and (b) V 2p spectra.

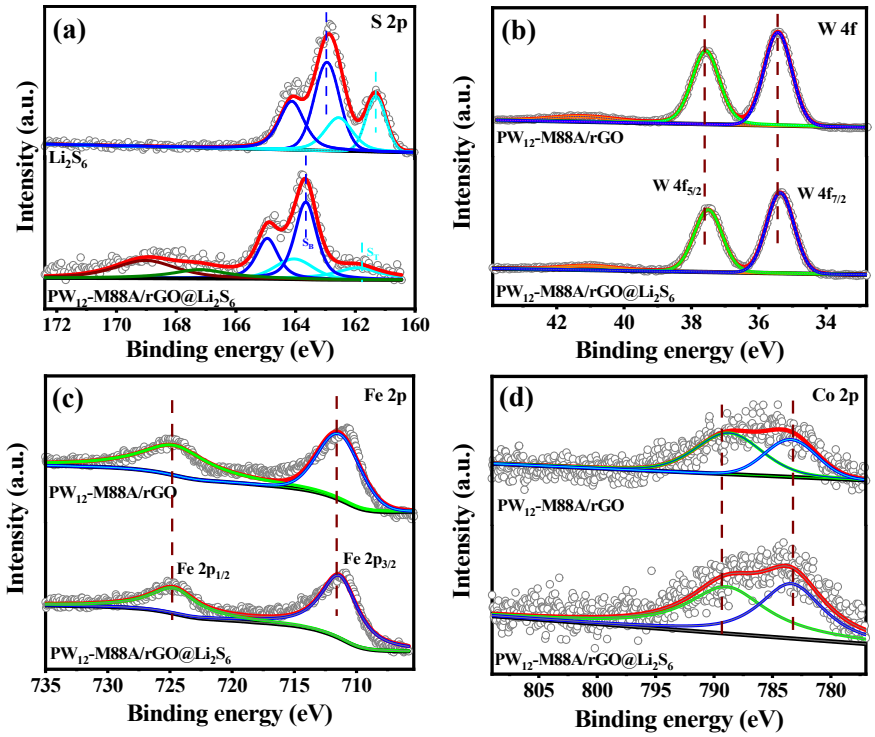

Fig. S15 (a) XPS analysis of S 2p spectra for bare Li_2S_6 and PW_{12}-M88A/rGO@Li_2S_6. XPS analysis of PW_{12}-M88A/rGO and PW_{12}-M88A/rGO@Li_2S_6: (b) W 4f spectra, (c) Fe 2p spectra, and (d) Co 2p spectra.

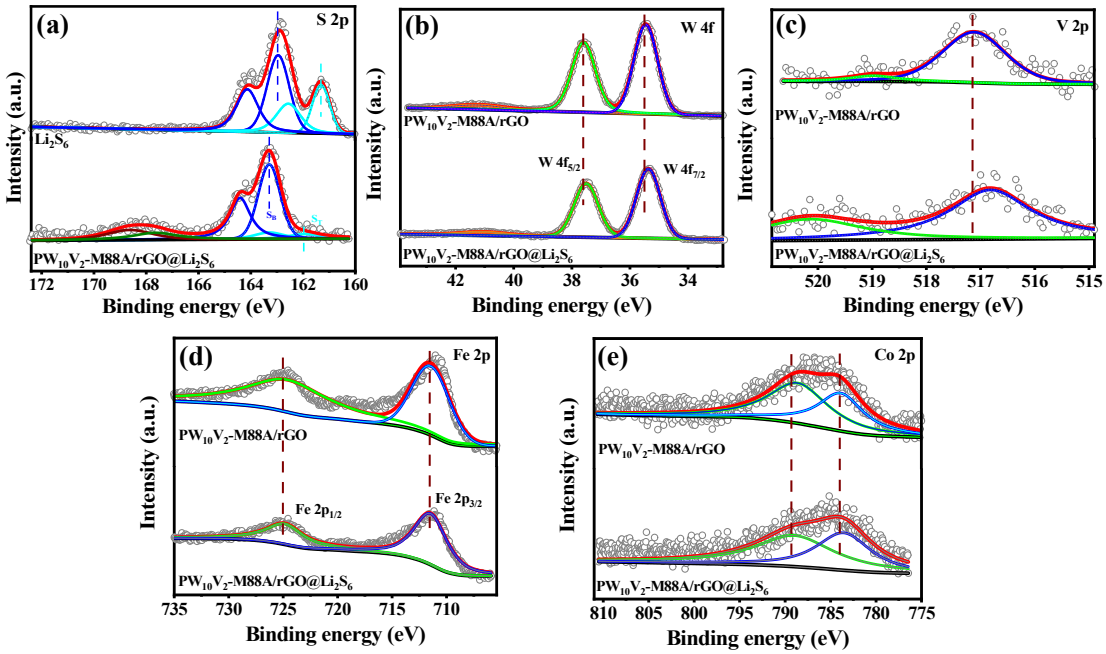

Fig. S16 (a) XPS analysis of S 2p spectra for bare Li_2S_6 and $PW_{10}V_2$-M88A/rGO@Li_2S_6. XPS analysis of $PW_{10}V_2$-M88A/rGO and $PW_{10}V_2$-M88A/rGO@Li_2S_6: (b) W 4f spectra, (c) V 2p spectra, (d) Fe 2p spectra, and (e) Co 2p spectra.

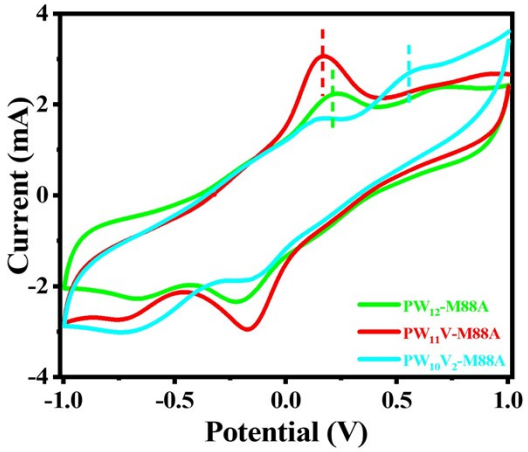

Fig. S17 CV curves of symmetrical cells at 10 mV s^{-1} with PW_{12}-M88A, $PW_{11}V$-M88A, and $PW_{10}V_2$-M88A working electrodes, respectively, and the electrolyte is 0.5 M Li_2S_6 solution.

$PW_{10}V_2$-M88A with more vanadium atoms presents the relatively strong oxidizability, which makes the catalytic oxidation of short-chain LiPSs into long-chain LiPSs more accessible during the charging process, corresponding to a higher oxidation potential. However, the collapse of hollow structure in $PW_{10}V_2$-M88A is not conducive to the enhancement of electrochemical performance. $PW_{11}V$-M88A with single vanadium atom implantation shows the suitable oxidizability (the oxidation potentials of $PW_{11}V$-M88A and PW_{12}-M88A are similar, both lower than that of $PW_{10}V_2$-M88A), which can not only ensure the integrity of hollow structure, but also further enhance the effective adsorption and catalysis of polysulfides by the substituted vanadium atom in $PW_{11}V$.

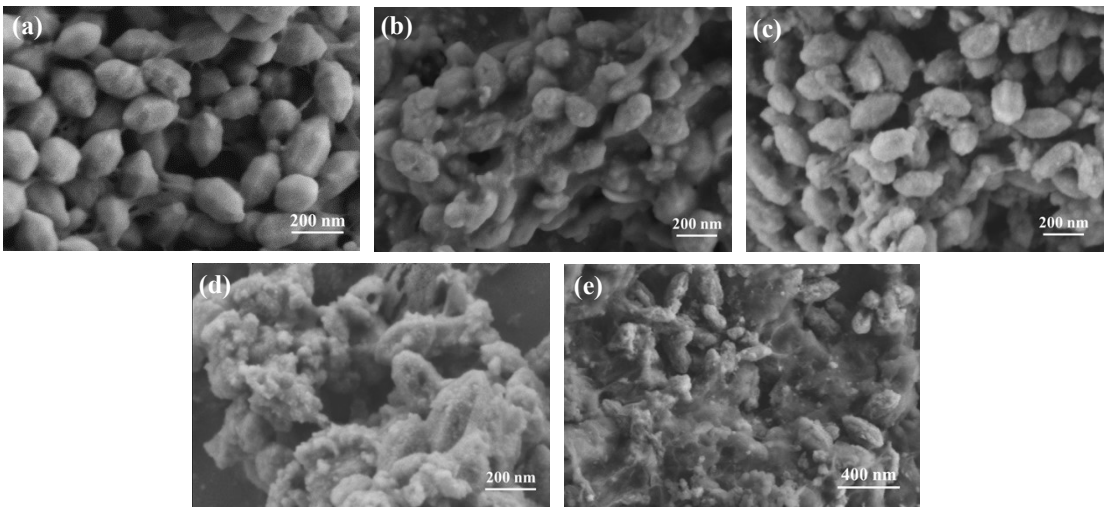

Fig. S18 SEM images of (a) M88A, (b) PW_{12}-M88A, (c) $PW_{11}V$-M88A, (d) $PW_{10}V_2$-M88A, and (e) $PW_{11}V$-M88A/rGO after catalytic reaction.

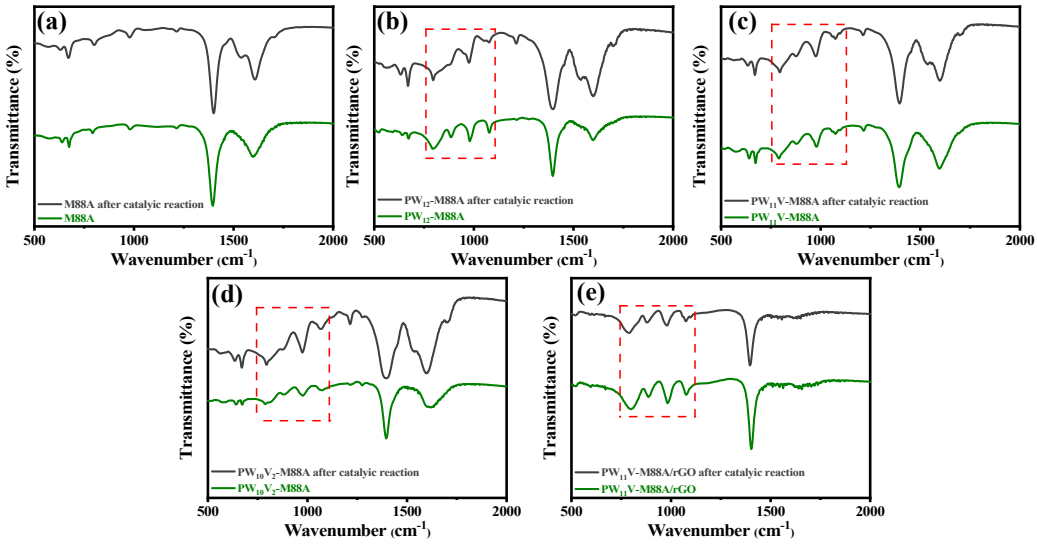

Fig. S19 FTIR spectra of (a) pristine M88A and M88A after catalytic reaction, (b) pristine PW_{12}-M88A and PW_{12}-M88A after catalytic reaction, (c) pristine $PW_{11}V$-M88A and $PW_{11}V$-M88A after catalytic reaction, (d) pristine $PW_{10}V_2$-M88A and $PW_{10}V_2$-M88A after catalytic reaction, and (e) pristine $PW_{11}V$-M88A/rGO and $PW_{11}V$-M88A/rGO after catalytic reaction.

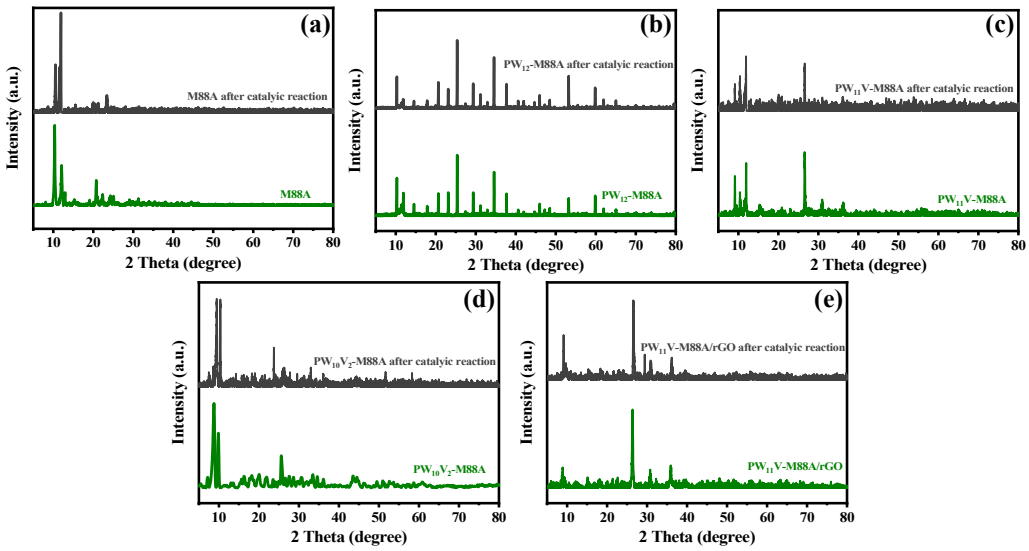

Fig. S20 XRD patterns of (a) pristine M88A and M88A after catalytic reaction, (b) pristine PW_{12}-M88A and PW_{12}-M88A after catalytic reaction, (c) pristine $PW_{11}V$-M88A and $PW_{11}V$-M88A after catalytic reaction, (d) pristine $PW_{10}V_2$-M88A and $PW_{10}V_2$-M88A after catalytic reaction, and (e) pristine $PW_{11}V$-M88A/rGO and $PW_{11}V$-M88A/rGO after catalytic reaction.

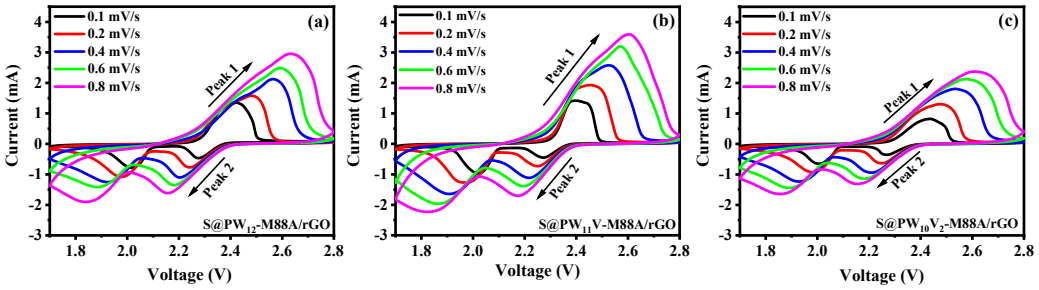

Fig. S21 The CV curves of (a) S@PW_{12}-M88A/rGO, (b) S@$PW_{11}V$-M88A/rGO, and (c) S@$PW_{10}V_2$-M88A/rGO at scan rate of 0.1, 0.2, 0.4, 0.6, and 0.8 mV s^{-1}. The coin cells are assembled with as-prepared samples as working electrodes, metallic lithium foil as the counter and reference electrodes, and 1 M LiTFSI in DOL/DME (1:1 by volume) with 1 wt% $LiNO_3$ as electrolyte.

Table S1. CHN results for PW_{12}-M88A/rGO, $PW_{11}V$-M88A/rGO, and $PW_{10}V_2$-M88A/rGO analyzed by CHN elemental analyzer.

Samples	C	H	N
PW_{12}-M88A/rGO	39.43%	0.69%	/
$PW_{11}V$-M88A/rGO	35.38%	0.76%	/
$PW_{10}V_2$-M88A/rGO	39.35%	0.74%	/

Table S2. P, W, V, Fe, and Co concentrations in PW_{12}-M88A/rGO, $PW_{11}V$-M88A/rGO, and $PW_{10}V_2$-M88A/rGO determined by ICP-OES analysis.

Samples	P	W	V	Fe	Co
PW_{12}-M88A/rGO	0.3302%	23.5203%	/	5.8854%	0.3096%
$PW_{11}V$-M88A/rGO	0.3652%	23.8464%	0.6009%	6.3480%	0.3341%
$PW_{10}V_2$-M88A/rGO	0.3529%	20.9442%	1.1610%	6.0782%	0.3199%

Table S3. Cycling performance of S@$PW_{11}V$-M88A/rGO compared with other previously reported sulfur cathodes with the representative catalysts in the literatures.

Sulfur host	Sulfur loading	Catalyst	Capacity decay rate per cycle (after n^{th} cycle)	Reference
C@TiN hollow spheres	71.00%	TiN	0.120% (150^{th}) at 1 C	[1]
Yolk-shelled Fe_3O_4@C	80.00%	Fe_3O_4	0.070% (200^{th}) at 0.1 C	[2]
NC/MoS_3-S NBs	70.00%	MoS_3	0.076% (500^{th}) at 0.5 C	[3]
$Fe_{3-x}C$@C-500	74.00%	$Fe_{3-x}C$	0.040% (1000^{th}) at 1 C	[4]
Graphene/TiN nanowires	80.00%	TiN	0.175% (200^{th}) at 1 C	[5]
N-CN-750@Co_3Se_4	61.50%	Co_3Se_4	0.067% (800^{th}) at 0.2 C	[6]
(N-doped porous carbon cage) NHSC	69.58%	NHSC	0.037% (500^{th}) at 1 C	[7]
C/Co_3O_4	66.00%	Co_3O_4	0.066% (500^{th}) at 0.5 C	[8]
C@TiN	70.00%	TiN	0.049% (300^{th}) at 2 C	[9]
TiB_2	71.00%	TiB_2	0.058% (500^{th}) at 1 C	[10]
MXene/1T-2H MoS_2-C	79.60%	1T-2H MoS_2	0.070% (300^{th}) at 2 C	[11]
δ-MnO_2	72.50%	δ-MnO_2	0.185% (200^{th}) at 0.06 C	[12]
NiO-$NiCo_2O_4$@C	73.00%	NiO-$NiCo_2O_4$	0.059% (500^{th}) at 0.5 C	[13]
CNTs/Co_3S_4-nanoboxes	70.00%	Co_3S_4	0.068% (500^{th}) at 2 C	[14]
$PW_{11}V$-M88A/rGO	70.00%	$PW_{11}V$	0.046% (500^{th}) at 3 C	This work

References

[1] Y. Wang, R. Zhang, Y. Pang, X. Chen, J. Lang, J. Xu, C. Xiao, H. Li, K. Xi and S. Ding, Energy Storage Mater., 2019, **16**, 228-235.

[2] J. He, L. Luo, Y. Chen and A. Manthiram, Adv. Mater., 2017, **29**, 1702707.

[3] J. Yu, J. Xiao, A. Li, Z. Yang, L. Zeng, Q. Zhang, Y. Zhu and L. Guo, Angew. Chem., Int. Ed., 2020, **59**, 13071-13078.

[4] Y. Zhang, G. Li, J. Wang, G. Cui, X. Wei, L. Shui, K. Kempa, G. Zhou, X. Wang and Z. Chen, Adv. Funct. Mater., 2020, **30**, 2001165.

[5] R. Wang, J. Yang, X. Chen, Y. Zhao, W. Zhao, G. Qian, S. Li, Y. Xiao, H. Chen, Y. Ye, G. Zhou and F. Pan, Adv. Energy Mater., 2020, **10**, 1903550.

[6] D. Cai, B. Liu, D. Zhu, D. Chen, M. Lu, J. Cao, Y. Wang, W. Huang, Y. Shao, H. Tu and W. Han, Adv. Energy Mater., 2020, **10**, 1904273.

[7] S. Zeng, G.M. Arumugam, X. Liu, Y. Yang, X. Li, H. Zhong, F. Guo and Y. Mai, Small, 2020, **16**, 2001027.

[8] F. Ma, J. Liang, T. Wang, X. Chen, Y. Fan, B. Hultman, H. Xie, J. Han, G. Wu and Q. Li, Nanoscale, 2018, **10**, 5634-5642.

[9] Y. Wang, R. Zhang, Y. Pang, X. Chen, J. Lang, J. Xu, C. Xiao, H. Li, K. Xi and S. Ding, Energy Storage Mater., 2019, **16**, 228-235.

[10] C. Li, X. Liu, L. Zhu, R. Huang, M. Zhao, L. Xu and Y. Qian, Chem. Mater., 2018, **30**, 6969-6977.

[11] Y. Zhang, Z. Mu, C. Yang, Z. Xu, S. Zhang, X. Zhang, Y. Li, J. Lai, Z. Sun, Y. Yang, Y. Chao, C. Li, X. Ge, W. Yang and S. Guo, Adv. Funct. Mater., 2018, **28**, 1707578.

[12] K. Cao, H. Liu, Y. Li, Y. Wang and L. Jiao, Energy Storage Mater., 2017, **9**, 78-84.

[13] L. Hu, C. Dai, H. Liu, Y. Li, B. Shen, Y. Chen, S.-J. Bao and M. Xu, Adv. Energy Mater., 2018, **8**, 1800709.

[14] T. Chen, Z. Zhang, B. Cheng, R. Chen, Y. Hu, L. Ma, G. Zhu, J. Liu and Z. Jin, J. Am. Chem. Soc., 2017, **139**, 12710-12715.